TURBULENCE CONTROL BY COMPLIANT SKIN AND STRATA-CORNEAS DESQUAMATION OF A SWIMMING DOLPHIN

Hiroshi Nagamine, Atsusi Taki, Tohru Murata, Yoshimichi Hagiwara
Department of Mechanical and System Engineering
Kyoto Institute of Technology,
Matsugasaki, Kyoto 606-8585, Japan
hnaga02@ipc.kit.ac.jp, yoshi@ipc.kit.ac.jp

Ryoichi Matsubara
Echizen-Matsushima Aquarium
Mikuni-cho, Sakai-gun, Fukui-ken 913-0065, Japan
aquarium@fki.fitweb.or.jp

ABSTRACT

Direct numerical simulation and experiment have been conducted for turbulent water flow near the compliant surface with the separation of pieces of the surface with time in order to examine how the turbulence control and drag reduction are performed by swimming dolphins. The surface is covered with many cluster models of beads and springs as representative of the strata corneas. The computational results show that the compliant surface contributes to the drag reduction. The separation of small pieces of the surface with time increases the Reynolds stress on average, which is verified by the experimental result. When the separation rate is high, however, the separation modifies near-wall turbulence and decreases the shear stress.

INTRODUCTION

Recent research in marine biology, naval engineering and fluid engineering has investigated in the reduction of skin friction by swimming dolphins. The relationship between this reduction and compliant skin was dealt with in a number of studies: Endo and Himeno (2002) and Xu et al. (2001) carried out direct numerical simulations on turbulent flows over compliant visco-elastic walls. They obtained turbulence control effects by the compliant walls.

However, part of the dolphin skin, in particular the back is hard and non-elastic, which is totally different from the soft skin on the ventral side of dolphins. The skin of swimming dolphins produces new cells every two hours approximately. The strata-corneas desquamation (the separation of small pieces of skin from the surface) of dolphins, which is related to the wall shear stress, has not yet been considered. Therefore, the key factor for the reduction of skin friction in swimming dolphins has not yet been clarified.

In the present study, we carry out a direct numerical simulation for turbulent flow near a compliant wall covered with many small pieces of the surface. The pieces are made of beads and connecting springs. The separation of the pieces from the compliant wall and interaction between the pieces and fluid flow are focused on in order to elucidate the effect of strata-cornea desquamation on the near-wall turbulence and the skin friction. We also conduct an experiment for turbulent water duct flow with a wavy wall covered with many small pieces of thin film to verify the simulation result.

COMPUTATIONAL METHOD

Assumptions for compliant surface

The deformation of the compliant surface was assumed to be sinusoidal in the streamwise direction, while remaining constant in the transverse direction at all times. The locations of nodes for the sinusoidal deformation were fixed. These assumptions are based on the observation of the ventral side of swimming bottlenose dolphins. Also, it was assumed that the wall between a node and the adjacent downstream node descends (ascends) when the wall shear stress in the narrow region along the node is higher (lower) than that in the narrow region along the downstream node at all time steps. The maximum displacement of descending (or ascending) was proportional to the difference in the wall shear stresses in these regions. The effect of pressure and the normal stress, whose values are lower than that of the shear stress, on the wall deformation was neglected.

Domains and schemes

Figure 1(a) shows the physical domain based on the assumption mentioned above. Both upper and lower walls of the domain deform in the same manner simultaneously. The lower wall is regarded as the compliant skin. The origin of the coordinates was at the corner of the lower wall. The x-, y- and z-axes were positioned in the streamwise, vertical and transverse directions, respectively. The deformation of the walls was one-period sinusoidal in the x direction. The locations of two nodes for the deformation were fixed. The streamwise dimension of the domain ($2\pi h^*$) changed in time

due to the deformation of the walls. The ξ- and η-axes were positioned along the wall and the wall-normal direction, respectively.

The physical domain was converted to the computational domain as shown in Fig. 1(b), which is a rectangular box of $2h \times 2h \times \pi h$ in a flow between two flat plates at the distance of $2h$, by using an unsteady generalized curvilinear coordinate (Hagiwara et al., 2002). Thus, these dimensions of the computational domain were unchanged. The origin of the coordinates for the computational domain was at the corner of the lower wall. The ξ-, η- and z-axes were positioned in the streamwise, wall-normal and transverse directions, respectively. The domain was divided into a total of $64 \times 97 \times 64$ cells. The cell dimension is identical both in the ξ and the z directions. It increases from the walls to the axis based on a hyperbolic tangent. The velocity components were assigned at the center of the cell surfaces (grid points for velocities), and the pressure and the external force were assigned at the center of the cell (grid points for forces). The dimensions of each stratum cornea were identical and based on the grid spacing in the ξ and z directions. Since the amplitude of the wall deformation was kept low, the generalized curvilinear coordinate was nearly the same as the Cartesian coordinate, and therefore, the staggered grid worked well. The Reynolds number based on h and the friction velocity for the flat plate, u_τ, was 150.

Although the upper wall is unrealistic for a swimming dolphin in water, it is necessary for defining values of the metrics in the coordinate transformation at the lower wall. The metrics for the locations just below the upper wall corresponds to those for the location just below lower wall. Note that these values are to be defined only when the wall deforms with time and no definition is necessary for the steady sinusoidal wall.

The computational schemes were the same as those in our previous study (Hagiwara et al., 2002). The second-order central difference scheme based on the interpolation method and that without the method were applied for the finite differencing of the convection terms and the viscous terms of the NS equations, respectively. The modified third-order Runge-Kutta method was adopted for the explicit time integration of the convection terms, the viscous terms and the external-force terms. The fractional-step method was used for the implicit time integration of the pressure terms.

Cluster model for strata cornea

Figure 2(a) demonstrates a typical microscopic image of strata corneas from a bottlenose dolphin (The actual size of the image is 1.9mm × 1.4mm). The strata corneas were obtained by rubbing the skin surface softly with a sanitary cotton wool after wiping away excess sea water from the surface of the dolphin. Although some strata corneas were agglomerated by the rubbing, the cornea is found to consist of agglomerated fibrous proteins. The agglomerated proteins resemble the highly entangled polyethylene oxide or the highly entangled polysaccharide (Hagiwara et al., 2002). Thus, we used the cluster models of beads, springs and dashpots, which had been used for the models of these polymers, as the representatives of the strata cornea. Note that the present model is smaller and stiffer than the previous models. Figure 2(b) illustrates the present cluster model, which consists of six beads of the same density as that of the fluid on a plane and thirteen connecting springs and dashpots of no volume in parallel. Each cluster model had dimensions of $9.8\nu/u_\tau \times 0.6\nu/u_\tau \times 4.91\nu/u_\tau$. Table 1 compares the parameters for the present cluster model with the other cluster models in our previous studies (Hagiwara, et al, 2000; Hagiwara et al, 2002). It is found from this table that the present model is smaller than the other models.

As far as the present authors know, there is no established method to describe a gradual separation of small pieces of the surface at the wall boundary. Thus, we used the following assumptions. Each model was embedded in the lower wall originally. It appeared only after the local wall shear stress at its original location exceeded a threshold for a certain period. In the present study, the threshold was set at $300\rho u_\tau^2$, and the period was $15\nu/u_\tau^2$. The velocity of the model was assumed to be zero when it appeared. Then, the model started to creep along the wall by the imbalance of the drag force for the beads and the restitution force of two springs and two dashpots, which connected the model to the wall (i.e. inner tissue). The length of the two imaginary springs was the same as that of the shortest springs in Fig. 2(b). Finally, the model was separated from the wall and released into the flow when the length of the imaginary springs exceeded 1.1 times of their initial length. This is a new development of the time-varying boundary with the piecewise separation from its surface.

Once the model is transported by the flow, a two-way-coupling interaction was used between a bead of the models and the flow: the Stokes drag force and the restitution force of the springs and dashpots act on the beads and the reaction force to the drag force acts on the flow as an external point force. The reaction force for each bead was distributed to eight neighboring grid points for forces by a spatial interpolation method. Similarly, the fluid velocity around a bead was calculated from the values at eight neighboring grid points for velocities by this interpolation.

Table 1 : Parameters of cluster model

Parameters	Present	Carrageenan	PEO
Bead radius	0.3	0.3	0.5
Bead number	6	128	128
Spring length	4.9	4.9	4.9
Spring const.	0.2	0.2	0.2
Dashpot coeffi.	0.05	0.03	-
Height of model	0.6	5.5	15.7

Computational conditions

Computations have been performed for three different conditions; (a) solid wall without cluster models, (b) deformable wall without cluster models, and (c) deformable wall with cluster models.

The database of channel flow with solid walls was adopted as the initial velocity field. A total of 4096 cluster models

were allocated side-by-side just below the lower wall at the initial state in case (c).

The nonslip boundary condition was imposed for the walls. The periodical boundary condition was applied for velocity, pressure and the cluster models in the ξ and z directions.

EXPERIMENT

Test section

Figure 3 shows the schematic of the test section in the developed region of the horizontal duct of 20mm in height and 160mm in width. The apparatus including this duct is the same as that used in our previous study (Hagiwara et al, 2000). The bottom wall of the test section was covered with a wavy plate made of aluminum. The streamwise length of the plate was 120 mm. Since it is difficult to change the amplitude of the wavy wall with time based on the measured shear stress, we adopted the wavy wall with fixed amplitude. The amplitude and the wave length for the wavy plate were 1.6 mm and 6.5 mm, respectively.

The measurement was performed in the following two cases; (d) the fixed wavy wall without gradual separation of small pieces from the surface, and (e) the fixed wavy wall with gradual separation of small pieces. In order to realize these conditions at the same time, small pieces of aluminum foil of 1×1 mm^2 were glued on the half of the wavy plate in the transverse direction by a water-soluble adhesive agent. It was confirmed that the small pieces were separated gradually as the adhesive agent was dissolved into the water flow.

A flush-mounted type of hot-film sensor (TSI type1237w) was used for the measurement of wall shear stress fluctuation. The hot-film gage is allocated on the edge surface of the rod of 2 mm in diameter in the sensor. The gage is coated with a thin quartz plate. The sensor was mounted on the bottom wall so that the surface of the quartz coating was flush with a crest of the wavy wall.

The sensor was connected to a constant-temperature anemometer (Kanomax Co. Ltd., model 1011). The analog output signal from the anemometer was stored into memory in a PC for 20s through an A/D conversion board. The sampling frequency of the conversion was 1 kHz.

Calibration

The relationship between the wall shear stress and the output voltage from the anemometer was calibrated by using turbulent flow in the identical duct with flat walls. The sensor was mounted so that the surface of the quartz coating was flush with the inner surface of the bottom wall.

The mean wall shear stress was evaluated from the measurement of mean velocity distribution of the flow. For this purpose, the flow was visualized by nylon 12 particles (specific weight: 1.02). The diameter of the particles was in the range of 0.1 – 0.2 mm. The upper limit of the frequency, beyond which these particles cannot respond to fluid fluctuation, was estimated to be about 75Hz from the result obtained by Hjelmfelt Jr. and Mockros (1966). This is higher than that of 25Hz, which is statistically reliable from the image-capturing rate and the sampling theorem.

Green light of Nd:YAG laser was used as the source of illumination light. The light was expanded with cylindrical lenses. Then, the expanded light was passed through a slit of 5 mm in width attached to the outside of the top wall.

Scattered light from the tracer particles was captured by a progressive-scan video camera (Sony, XC-8500CE). The capturing rate was 50 frames per second. The area for the full frame image was 0.050×0.038 m^2. Each pixel covered a square of 0.065×0.065 mm^2 in the observing field.

Improvement of the captured images was carried out before the image processing. First, the nonuniformity of the shading for the background of the digital images was compensated for by using a reference frame. Then, the neighborhood averaging technique was used for the smoothing of the images. Finally, binarization was carried out to enhance the particle images.

A particle-tracking-velocimetry (PTV) technique was applied for the preprocessed images. The particle velocity was estimated from the particle locations on four successive frames. The velocities of the tracer particles were redistributed to the 78×56 grid points allocated uniformly on the images by the interpolation method.

EXPERIMENTAL RESULTS AND DISCUSSION

Approximately 7 % increase in the mean shear stress was measured for the case with the separation of small pieces of the surface compared with that without the separation.

Figure 4 shows typical examples of time-traces of wall shear stress. It is found by comparing these traces that the fluctuation of the wall shear stress became noticeably by the separation of small pieces. It can be considered that the separating small peaces acted as a roughness to the flow, which induced the increase in the wall shear stress.

NUMERICAL RESULTS AND DISCUSSION

Turbulence statistics

The following turbulence statistics are based on the average values in the (ξ, z)-plane for the period from $450\nu/u_\tau^2$ to $1500\nu/u_\tau^2$.

Mean velocity. Figure 5 indicates the mean velocity profile. In the buffer layer, the mean velocity in the case of deformable wall without cluster models is lower than that of the solid wall case. The mean velocity in the case of deformable wall with cluster models is lower than the other two cases mentioned above. In the log region, on the other hand, the velocity in the case with cluster models is the highest among the three cases.

Turbulence intensities. Figure 6 shows the turbulence intensities. The streamwise intensity in the buffer region in the case of deformable wall without cluster models is higher than those in the case of the solid wall. The intensity in the case with cluster models is the highest among the three cases. The wall-normal and transverse intensities are lower than those in the case without cluster models or those of the solid wall except for the maximum of the streamwise intensity in the buffer layer. This suggests that the redistribution mechanism of turbulent kinetic energy is affected by the wall deformation and the cluster models.

Shear stresses. Figure 7 depicts the shear stress profiles. The Reynolds shear stress and the total shear stress in the case of deformable wall without cluster models are lower than those of channel flow. On the other hand, these stresses in the case of the deformable wall with cluster models are higher than those in the case without cluster models. This is in qualitative agreement with our experimental result. It can be emphasized that these stresses in the case of deformable wall with cluster models for the early period from $300\nu/u_\tau^2$ to $600\nu/u_\tau^2$ are the lowest among all the cases. The highest rate of the separation of the cluster models was obtained during this period.

Judging from Figs. 5, 6 and 7, the method of wall deformation based on the difference in the wall shear stresses in the specific regions is effective for the reduction of space-temporal average of wall shear stress. The separation of small pieces of the surface is not effective for the reduction of the wall shear stress except during the period when there is a high rate of separation. The mechanism for the turbulence modification is discussed with some snapshots in the following section.

Hairpin vortices and wall shear stress contours

In the case without the cluster models. Figures 8(a) and 8(b) demonstrate a snapshot of the top view of hairpin vortices and the contour map of wall shear stress in the region including one node in the case of the deformable wall without the cluster models, respectively. Figure 8(c) shows low-speed streaks in white and the cross section of the vortices in gray on the (η, z)-plane at the node. At this moment, the wall was ascending in this region. The hairpin vortices were identified by the iso-surfaces of negative λ_2, the second largest eigenvalue of the tensor $S_{ik}S_{kj} + \Omega_{ik}\Omega_{kj}$, where S_{ij} and Ω_{ij} are the symmetric and antisymmetric parts of $\partial u_i/\partial x_j$, respectively (Jeong, et al., 1997). The black area indicates a high shear stress region, while the white area indicates a low shear stress region in Fig. 8(b). The number density of the hairpin vortices is low in the right-hand side of Fig. 8(a). This is caused by the suppression of the vortices by the main flow approaching the ascending wall. The evolution of the vortices and the ejection of the low-speed streaks were attenuated by this suppression. This is the main reason for the low number density of the vortices and thus the decrease in the shear stress.

In the case with the cluster models. Figures 9(a) and 9(b) show a snapshot of hairpin vortices and the contour map of wall shear stress for the same region as that in Fig. 8 in the case of deformable wall with the cluster models, respectively. Figure 9(c) shows high speed streaks in black and the cross section of the vortices in gray on the same (η, z)-plane as that in Fig. 8(c). At this moment, the wall was descending in this region. The hairpin vortices are found to be distributed more uniformly in Fig. 9(a) than that shown in Fig. 8(a). The higher wall shear stress regions in Fig. 9(b) are more noticeable than those in Fig. 8(b), which is in agreement with the experimental result mentioned above.

The black dots in Fig. 9(b) represent the beads of the cluster models. Note that the size of the beads is much larger than the actual size. Several cluster models are found to be transported by the high-speed streaks. The wallward motion of the streaks and therefore the Q4 event were enhanced by the models. This is the reason for the increase in the wall shear stress by the cluster models on average.

Figure 10 shows a typical snapshot of a (η, z)-plane during the period of high rate of the model separation. Many models are found to be concentrated in the buffer region, and they directly interacted with the hairpin vortices nearby and attenuated them. This is the reason for the reduction of the Reynolds shear stress during this period.

CONCLUSIONS

The direct numerical simulation was carried out for turbulent flow near the deforming wall with many cluster models of beads, springs and dashpots representing strata corneas separating from the surfaces. The experiment was also carried out with the wavy wall covered with small pieces of thin foil. The main conclusions are as follows.

1. The wall shear stress and the total shear stress are decreased by the wall deformation. This is mainly because the evolution of hairpin vortices is attenuated by the main flow approaching the ascending wall.
2. The separation of small pieces of the surface increases the Reynolds shear stress because the pieces interacted with the high-speed streaks. However, in the case of high rate of separation of these pieces, they directly attenuated near-surface coherent structure, thus shear stress on the surface.
3. The increase in the wall shear stress by the separation of small pieces of foil from the wavy surface was measured. This confirms the numerical results.

Acknowledgement

The authors acknowledge Mr. K. Yamahata for his assistance with this experiment.

REFERENCES

Endo, T. and Himeno, R., 2002, "Direct numerical simulation of turbulent flow over a compliant surface", *J. Turbulence*, Vol. 3, article no. 007.

Hagiwara, Y., et al., 2000, "Numerical simulation of the interactions of highly entangled polymers with coherent structure in a turbulent channel flow", *Int. J. Heat and Fluid Flow*, Vol.21, pp.589-598.

Hagiwara, Y. et al., 2002, "The modification of coherent structure along a waving film by polymer exudation in turbulent water flow", *J. Turbulence*, Vol. 3, article no. 010.

Hjelmfelt Jr, A. T., and Mockros, L. F., 1966, "Motion of discrete particles in a turbulent fluid", *Applied Scientific Research*, Vol.16, pp.149-161.

Jeong, J. et al., 1997, "Coherent structure near the wall in a turbulent channel flow", *J. Fluid Mechanics*, Vol.332, pp. 185-214.

Xu S. et al., 2001, "Direct numerical simulation of the interaction of near-wall turbulence with a compliant wall", Abstract of *IUTAM Symposium on Flow in Collapsible Tubes and Past other Highly Complaint Boundaries.*

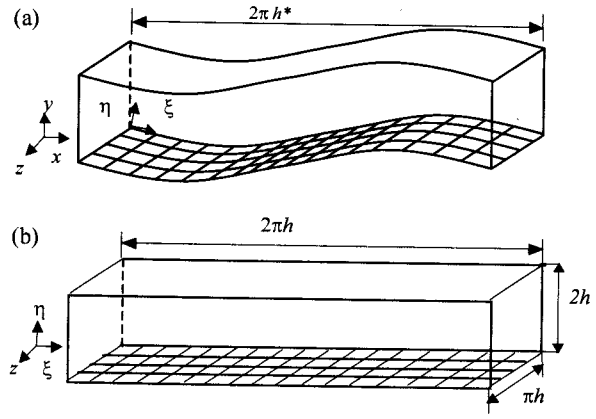

Fig. 1 Physical domain and computational domain

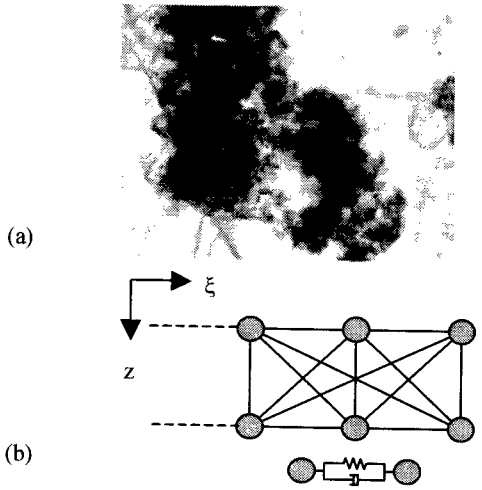

Fig. 2 Microscopic view of agglomerated strata-corneas and cluster model

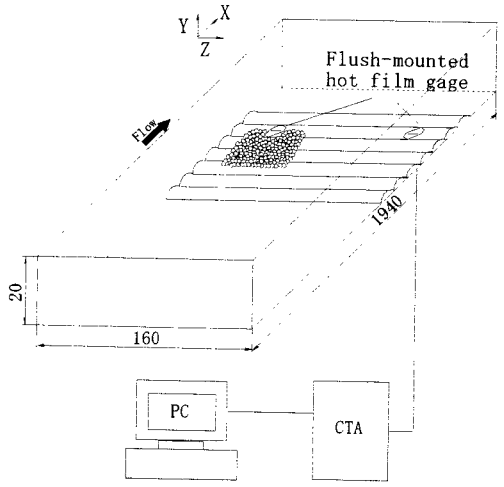

Fig. 3 Test section and signal recording system

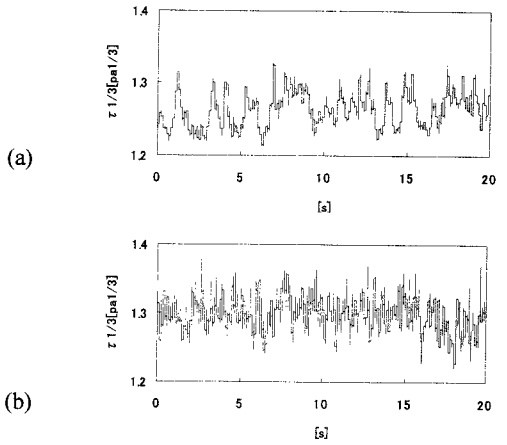

Fig. 4 Time traces of wall shear stress (a) without separation, (b) with separation.

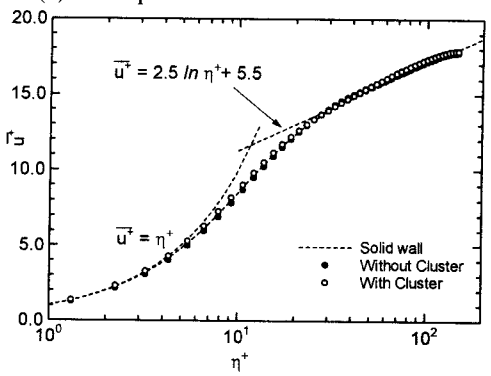

Fig. 5 Mean velocity profile

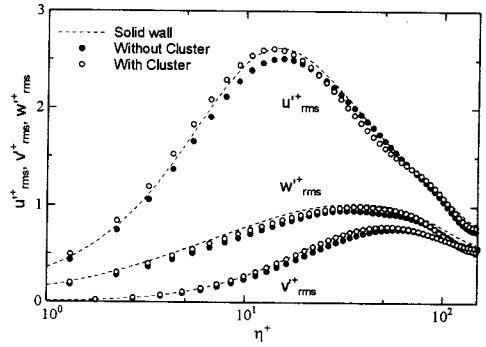

Fig. 6 Turbulence intensities

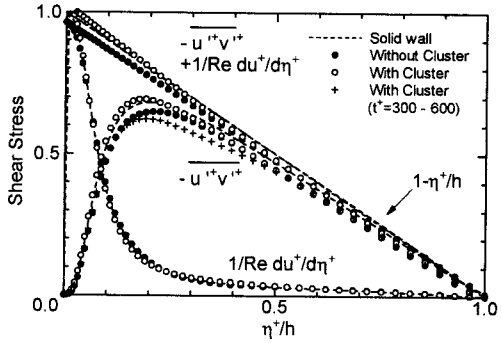

Fig. 7 Shear stresses

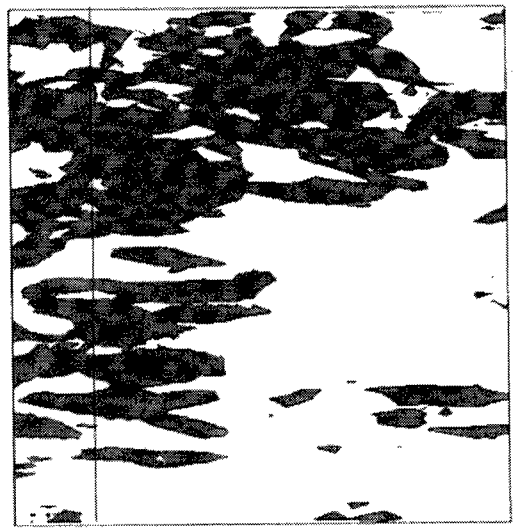

(a)

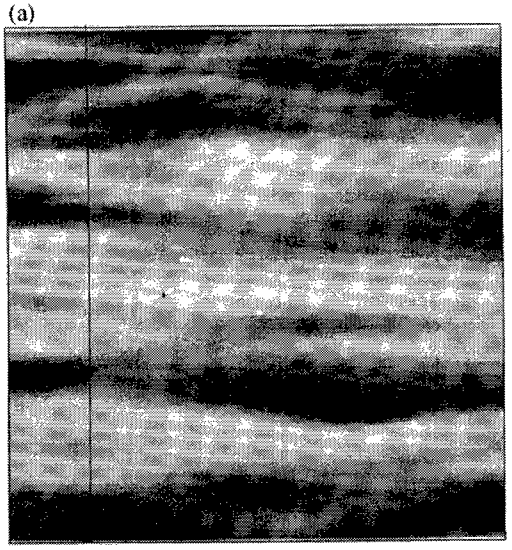

(b)

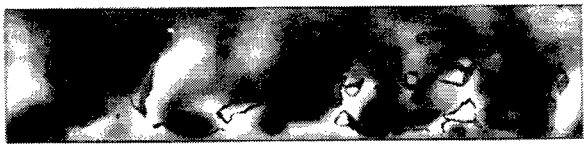

(c)

Fig. 8 Snapshot in the case without cluster models (a) hairpin vortices in top view ($471v/u_\tau \times 471v/u_\tau$), (b) contour of wall shear stress, (c) low-speed streaks and cross section (vertical line in (a)) of vortices in side view ($100v/u_\tau \times 471v/u_\tau$)

(a)

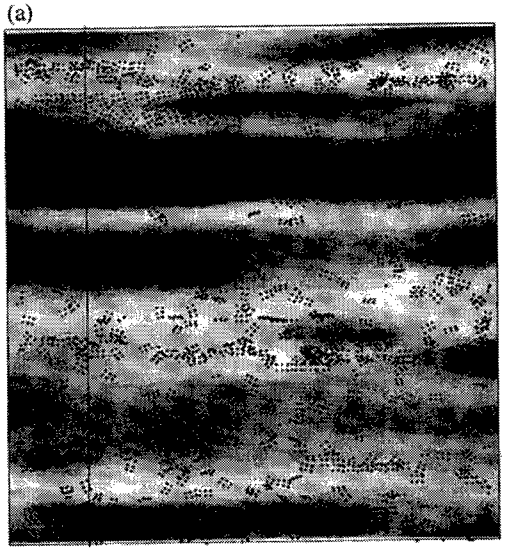

(b)

(c)

Fig. 9 Snapshot in the case with cluster models (a) hairpin vortices in top view ($471v/u_\tau \times 471v/u_\tau$), (b) contour of wall shear stress and models, (c) high-speed streaks, models and cross section (vertical line in (a)) of vortices in side view ($100v/u_\tau \times 471v/u_\tau$)

Fig. 10 High-speed streaks, models and cross section of vortices in side view ($100v/u_\tau \times 471v/u_\tau$) in early stage